

ARTICLE OPEN



Parallel InAs nanowires for Cooper pair splitters with Coulomb repulsion

Olivér Kürtössy^{1,2}, Zoltán Scherübl^{1,2,3}, Gergő Fülöp^{1,2}, István Endre Lukács⁴, Thomas Kanne⁵, Jesper Nygård⁵, Péter Makk^{1,6} and Szabolcs Csonka^{1,2}

Hybrid nanostructures consisting of two parallel InAs nanowires connected by an epitaxially grown superconductor (SC) shell recently became available. Due to the defect-free SC-semiconductor interface and the two quasi-one-dimensional channels being close by, these platforms can be utilized to spatially separate entangled pairs of electrons by using quantum dots (QD) in the so-called Cooper pair splitting (CPS) process. The minimized distance between the QDs overcomes the limitations of single-wire-based geometries and can boost the splitting efficiency. Here we investigate CPS in such a device where strong inter-dot Coulomb repulsion is also present and studied thoroughly. We analyze theoretically the slight reduction of the CPS efficiency imposed by the Coulomb interaction and compare it to the experiments. Despite the competition between crossed Andreev reflection (CAR) and inter-wire capacitance, a significant CPS signal is observed indicating the dominance of the superconducting coupling. Our results demonstrate that the application of parallel InAs nanowires with epitaxial SC is a promising route for the realization of parafermionic states relying on enhanced CAR between the wires.

npj Quantum Materials (2022)7:88; <https://doi.org/10.1038/s41535-022-00497-9>

INTRODUCTION

Nowadays superconducting nanostructures built from InAs nanowires attract huge attention in the field of quantum electronics. Beyond being a versatile platform to investigate the spatial separation of entangled electrons originating from a SC via QDs, namely CPS^{1–3}, they are also promising candidates to host such systems as Andreev-qubits^{4–8} or topologically protected bound states, e.g. Majorana fermions (MF)^{9–13}. Although single-wire circuits have already been realized to study MFs^{14–20} and CPS^{21–26}, latest theoretical research even predicts non-Abelian anyons with more exotic statistics, so-called parafermions, to appear in devices built from two parallel nanowires^{27–29}. It is theorized that Z3 parafermions can arise in a pair of tightly placed wires with a joint SC by exploiting the CAR and the Coulomb interaction^{2,30,31}. As a natural indication of the strong SC-mediated coupling, one might expect the enhancement of CPS in such an arrangement as the distance (δr) between the two points where the split electrons are injected into the parallel QDs can be substantially decreased (see Fig. 1a, b)^{1,32}.

Besides CPS is intensively researched in several other platforms, e.g. in graphene-based junctions^{33–36}, it has been also reported in individual nanowires placed manually next to each other and connected via an ex-situ deposited Al contact^{37,38}. However, hybrid nanostructures became available recently, where double InAs nanowires are grown in close vicinity and are connected by an in-situ evaporated SC Al (see Fig. 1c)^{39–44}. The latter property can satisfy a set of strict requirements from the geometry: the direct tunneling between the QDs is prevented^{45,46}, and the SC-nanowire interface becomes high-quality^{47,48}, rendering them a suitable platform for CPS circuits. As a result of the minimal distance of QDs preferred for the CPS in such setups, the inter-dot

Coulomb repulsion (U_{LR}) also becomes considerable (see Fig. 1b). This parasitic effect competes with the SC-induced inter-wire transport processes, where two electrons are transmitted through the adjacent QDs. Although previous theoretical works have investigated the mechanism of CPS in parallel double QD systems, they either neglected the impact of the inter-dot capacitance^{49–51}, or focused on the regime of strong coupling to the SC (Andreev limit)^{13,52–62}, the opposite of what is desired for CPS^{1,63}.

In this paper, we report a significant CPS signal observed in parallel InAs nanowires with an epitaxial Al layer. We discuss the CPS through a parallel double QD system and estimate the relative reduction of its efficiency in the presence of finite inter-dot Coulomb repulsion energies. Despite the strength of this capacitive coupling being comparable to the superconducting gap (Δ) in our experiments, we report a higher splitting efficiency than in most preceding experiments performed in InAs nanowires. Our findings demonstrate that double nanowires with epitaxial SC are ideal for future applications, where the dominance of crossed Andreev processes is needed^{27–29}.

RESULTS

Device outline & setup

The system studied here is illustrated in Fig. 1b–e. Pairs of parallel InAs nanowires were grown in close proximity as discussed in ref. 39 (see panel c). An epitaxial Al layer was deposited in-situ (blue in panels d, e) merging them by covering 2 facets as displayed by a transmission electron microscopy (TEM) image in the top right of Fig. 1c. After transferring a pair of wires to a substrate, the Al was partially removed from them (brown) by using a wet etch method (for details, see Appendix)³⁹. Two normal

¹Department of Physics, Institute of Physics, Budapest University of Technology and Economics, Műegyetem rkp. 3, H-1111 Budapest, Hungary. ²MTA-BME Nanoelectronics Momentum Research Group, Műegyetem rkp. 3, H-1111 Budapest, Hungary. ³University Grenoble Alpes, CEA, Grenoble INP, IRIG, PHELIQS, 38000 Grenoble, France. ⁴Center for Energy Research, Institute of Technical Physics and Material Science, Konkoly-Thege Miklós út 29–33., H-1121 Budapest, Hungary. ⁵Center for Quantum Devices, Niels Bohr Institute, University of Copenhagen, 2100 Copenhagen, Denmark. ⁶MTA-BME Correlated van der Waals Structures Momentum Research Group, Műegyetem rkp. 3, H-1111 Budapest, Hungary. ✉email: okurtossy@edu.bme.hu; makk.peter@ttk.bme.hu; csonka.szabolcs@ttk.bme.hu

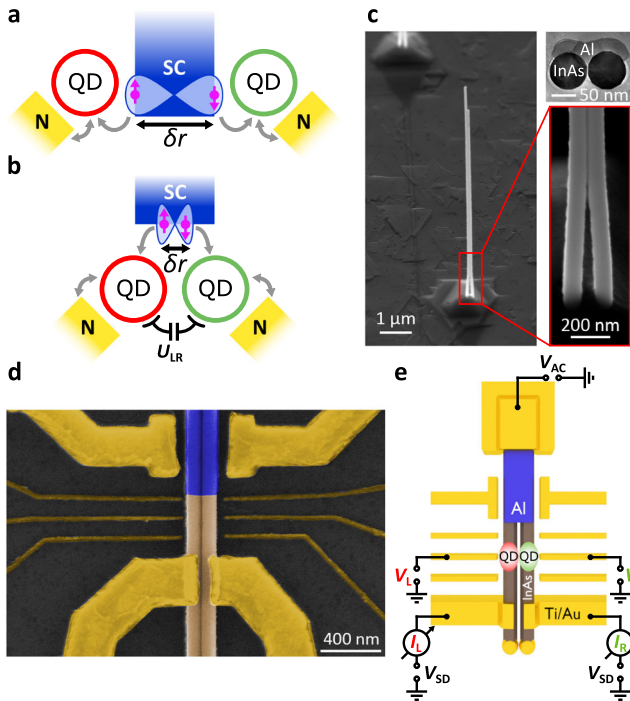


Fig. 1 Device outline. **a** Concept of a single-nanowire based Cooper pair splitter. Lower bound for δr is the width of the SC with negligible cross-capacitance between the QDs. **b** Same as panel (a), but in double, parallel nanowires. While δr can be minimized, U_{LR} becomes significant. **c** High-resolution SEM micrographs of the as-grown nanowires imaged from the opposite side of the Al covering. A TEM image on the top shows the cross-section of the material with the Al connecting the two InAs wires. **d** False-colored scanning electron microscopy (SEM) image of the device. The epitaxial Al (blue) was etched away from half of the InAs nanowires (brown). Two separate and a shared Ti/Au contacts and side gate electrodes (yellow) were evaporated to control the transport. **e** Schematic illustration of the measurement setup. The left (red) and right (green) QDs were tuned by V_L and V_R , respectively, and were biased simultaneously by V_{SD} . The currents in the two arms were measured via I/V converters, yielding the differential conductance G_L and G_R .

metal electrodes (Ti/Au, yellow) were formed to the etched segments contacting the wires separately, while a third normal electrode was evaporated on the epitaxial SC (see Fig. 1e) with a distance of $\sim 2 \mu\text{m}$ measured from the border of the etching. We note that this length exceeds the superconducting coherence length of the Al (ξ). Additional 3-3 side gate electrodes were defined to create electrostatically a QD in each of the wires, thus obtaining parallel SC-QD-N junctions with a joint SC (N stands for normal metal). Low-temperature electronic transport measurements were carried out at a base temperature of 40 mK.

Tunnel barriers were formed by adjusting the voltage on the outer side gates. If the coupling of the QDs is stronger to the SC than to the normal leads, sub-gap states can be formed and one enters the Andreev limit^{13,52–56,58,61,62}. In our case, the tunnel barriers were set such that the opposite limit was reached, where the normal leads were coupled strongly. This allowed the QDs to be emptied rapidly without blocking the transport, hence making it suitable to investigate CPS^{1,63}. The middle finger gate electrodes served as plunger gates to tune the level position of the left (red) and right (green) QDs by V_L and V_R , respectively (see Fig. 1e). Differential conductance $G_L = dI_L/dV_{AC}$ and $G_R = dI_R/dV_{AC}$ through the left and right QDs were recorded on the normal contacts biased by V_{SD} applied on the offset inputs of home-built I/V converters. With this geometry, we minimized δr in order to boost the superconducting inter-dot correlations as suggested

in refs. 1,32, since the CPS current (ΔI) is suppressed as:

$$\Delta I \propto \exp\{-2\delta r/\pi\xi\}, \quad (1)$$

however, we also introduced a finite U_{LR} at the same time, as shown in Fig. 1b.

Experiments

In the following, we discuss the spectrum of the created double QD system. Figure 2a, b show the zero-bias conductance of the left and right QDs, respectively, as a function of the two plunger gate voltages in the normal state reached by $B = 250$ mT out-of-plane magnetic field. The finite slopes of the lines are attributed to the capacitance between the left (right) plunger gate and the right (left) QD. The resonance lines of each QD shift in the phase diagram when the other one is being charged (or discharged) due to the significant inter-dot Coulomb repulsion, resulting in an effective gating and exhibiting a honeycomb pattern, which is well-known for capacitively coupled double QDs⁶⁴. Figure 2c, d show normal-state finite-bias spectroscopy of the left and right QDs performed along the white and gray dotted line in Fig. 2a, b, while Fig. 2e, f show the same measurements in the superconducting state ($B = 0$). The charging energies of the left and right QDs were extracted from the size of the Coulomb-diamonds as $U_L = 0.9$ meV and $U_R = 0.7$ meV, while the total couplings were estimated from the level broadenings as $\Gamma_L \approx 0.28$ meV and $\Gamma_R \approx 0.45$ meV, respectively. Here $\Gamma_{L(R)} = \Gamma_{SL(R)} + \Gamma_{NL(R)}$ and $\Gamma_{SL(R)}$ describes the tunnel rate between the SC and the left(right) QD, while $\Gamma_{NL(R)}$ is the tunnel rate between the left (right) QD and the normal lead. The strength of the inter-dot Coulomb repulsion was found to be $U_{LR} = 0.15$ meV estimated from the relative shift of the resonance lines in Fig. 2a, b⁶⁴. In Fig. 2e, f the Coulomb resonances split up at zero bias and a soft gap opens with 2Δ energy in the excitation spectra (with $\Delta = 0.15$ meV), typical for SC-QD-N junctions. The tip of the diamonds also shift in gate voltage and the lack of sub-gap states confirms the weak coupling towards the SC ($\Gamma_{SL(R)} \ll \Gamma_{NL(R)}$), needed for CPS experiments.

Let us now explore the zero-bias conductance of the QDs from Fig. 2a, b, but in the superconducting state. The corresponding charge stability maps are shown in Fig. 3a, b. Here the conductance of both QDs is smaller globally compared to Fig. 2a, b, but non-zero due to the presence of the soft gap. In contrast to the normal-state data where the capacitive cross-talk yields minima at the intersections of the left and right QD resonances, in the superconducting state, maxima develop instead. These are manifested in Fig. 3b by the yellow spots at the shifting resonance lines. To prove that CPS takes place in our system and to quantify its efficiency, we focus on the evolution of the signal amplitudes along single resonance lines. In Fig. 3c G_L and G_R are plotted along a resonance of the right QD, whose trace is depicted with the blue dashed line in Fig. 3a, b. The red curve shows the resonances of the left QD, and we call this signal "local", whereas the green one shows the changes in the conductance of the right QD as a function of V_L , hence we denote this as the "non-local" signal. Although G_R is always maximal along this cut, well-pronounced peaks emerge when the left QD is also brought to resonance. Similarly, in Fig. 3d, where the roles of QDs are interchanged, G_L and G_R are demonstrated along the pink dashed line from Fig. 3a, b. Here one can see a significant increase in the left QD signal when the right QD becomes resonant as well. E.g. the non-local peaks at $V_L = 3.24$ V and $V_R = 0.07$ V can be recognized in both QD signals in Fig. 3c, d with the equal height of ΔG indicated by the black arrows. These non-local maxima vanish by switching off the superconductivity as shown in Fig. 3e, f, where the same analysis was carried out as in Fig. 3c, d but in the normal state along the blue and pink dotted lines in Fig. 2a, b. In the absence of superconductivity, the overall conductivity increases, and the non-local peaks are replaced by dips. These features are robust along

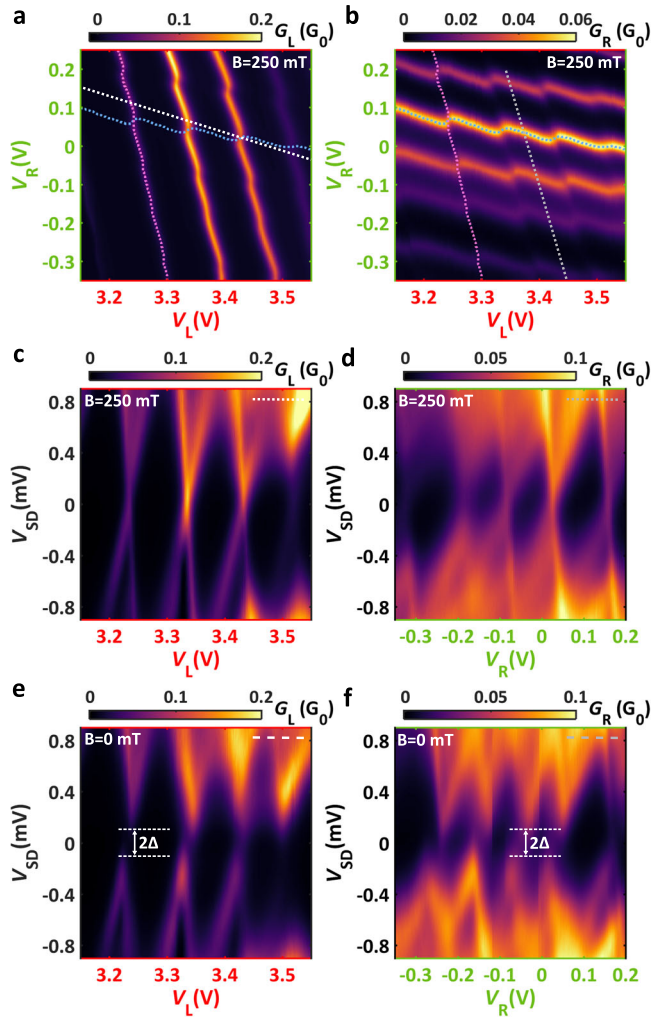


Fig. 2 QD characterization. **a, b** Zero-bias stability maps of the left and right QDs in the normal state. Finite capacitance between the plunger gates to the opposite QDs with the strong inter-dot Coulomb repulsion establishes a honeycomb structure in the phase diagram. **c, d** Bias spectroscopy of the left and right QDs in the normal state and **e, f** in the superconducting state along the white and gray dotted lines in panels (**a, b**). $U_{LR} = 0.15$ meV was read off from the phase diagram, while charging energies of the left and right QDs were extracted as $U_L = 0.9$ meV and $U_R = 0.7$ meV, respectively, with $\Delta = 0.15$ meV from the Coulomb-blockade spectroscopy. The couplings were estimated to be $\Gamma_L \approx 0.28$ meV and $\Gamma_R \approx 0.45$ meV.

each resonance (for additional data, see Supplementary Note 1). We emphasize that the dips are much deeper than what is expected from resistive cross-talk introduced in ref. ²¹, and they are caused by the finite inter-dot capacitance, which penalizes the simultaneous electron occupation of the adjacent QDs. The strong positive correlation only existing in the superconducting state demonstrates the presence of robust CPS.

The CPS efficiency can be defined as $s = 2\Delta G / (G_L + G_R)$, while visibility of the non-local signal in the left (right) QD is $\eta_{L(R)} = \Delta G / G_{L(R)}$, where ΔG is the non-local signal amplitude equal in the two wires (see Fig. 3c, d)^{21,24,37,46}. We estimated the maximal and average CPS efficiency as $s_{\max} = 29$ –36% (see the white arrow in Fig. 3a, b) and $\bar{s} = 19$ –28% in the investigated gate range, respectively. The maximal visibility was found to be $\eta_{L,\max} = 40$ –49% and $\eta_{R,\max} = 29$ –40% (see the gray arrow in Fig. 3a, b). The lower bounds of the given ranges are derived as ΔG being measured from the baseline of the resonances. More realistic

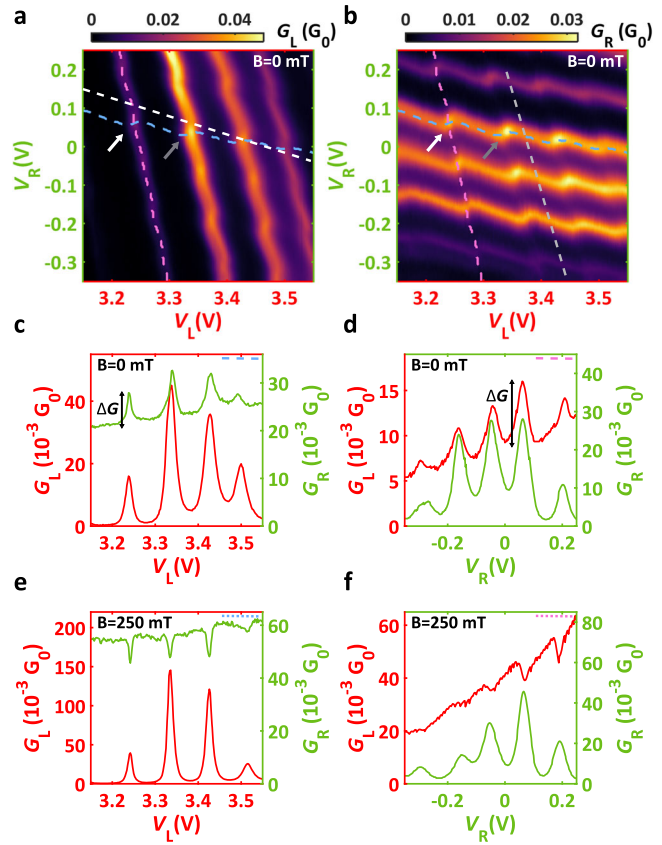


Fig. 3 CPS validation. **a, b** Same gate stability maps as in Fig. 2a, b, but in the superconducting state. The white and gray arrows show the spots with the maximal splitting efficiency and maximal visibility of the non-local signal, respectively. **c** Conductance along a selected resonance of the right QD indicated by the blue dashed line in panels (**a, b**). There is a strong positive correlation between G_L and G_R . **d** Similar cut to panel (**c**), but along a resonance of the left QD shown by the pink dashed line in panels (**a, b**). The peaks at $V_L = 3.24$ V match the one at $V_R = 0.07$ V in panel (**c**) with the same amplitude of ΔG . **e, f** Normal state data of the corresponding cuts in panels (**c, d**) (taken along the pink and blue dotted lines in Fig. 2a, b). Once the superconductivity is suppressed by external magnetic field, negative correlations overtake the non-local peaks arising from the non-negligible U_{LR} .

estimates (used here as upper bounds) are calculated by considering the relative reduction of the conductance usually reaching 15% (see Fig. 3e, f), which is always present in the system as it comes from the capacitive coupling. In this case, the CPS signals are estimated by the sum of the previously described ΔG and the expected depth of the dips in the QD with smaller average conductance in the superconducting state. Here the condition of the non-local signals being equal in G_L and G_R is still satisfied, however, these numbers could even increase, if one takes into account higher-order processes, where the electrons of a Cooper pair split into different QDs finally leave to the same electrode^{24,45}. In the following, we explore the relative reduction of these quantities caused by the Coulomb interaction between the QDs.

DISCUSSION

A finite U_{LR} is expected to quench the CPS as it penalizes transport processes where both QDs are being charged simultaneously. To confirm this assumption and to quantify this effect, we developed

a rate equation model to calculate the relative CPS currents in parallel QDs at different electron occupations.

The QDs are treated as single sites in the frame of the Anderson model with $\delta r = 0$. We use the notation $|m, n\rangle$ for $|m\rangle_L \otimes |n\rangle_R$ describing the ground state electron filling of the left and right QDs, where $m, n = \{0, \uparrow, \downarrow, 2\}$. The SC and the normal leads are handled by BCS density of states and Fermi distributions, respectively. All tunnel couplings are assumed to be weak compared to the governing energy scales ($U_{L(R)}, \Delta$)⁵⁰, and the transport is entirely described by transition rates determined by 4th order perturbation theory with Fermi's golden rule. The net current in the left (right) lead is obtained by solving the classical master equation in the stationary limit (for further details, see Supplementary Note 3).

Among the various transport mechanisms available in the system we distinguish local pair tunneling (LPT) and CPS in the calculations. A sequence of electron tunnelings is treated as LPT if the electrons constituting the Cooper pair leave the SC to the same QD, while the transport is considered to be CPS if the split electrons exit to separate QDs. One example for each of them is demonstrated in Fig. 4a where the order of the events in the sequence is indicated by black arrows and numbers. In both processes the initial and final states have the $|\uparrow, 0\rangle$ character, however, electrons with opposite spins arrive in the same leads at the end of a LPT, while they appear in separate arms in case of CPS (for a detailed discussion see Supplementary Note 3).

Intuitively, one expects the CPS efficiency to be maximal when both QDs are close to their resonances¹. This condition is satisfied in the vicinity of the degeneracy line of the $|1, 0\rangle$ and $|0, 1\rangle$ sectors in the phase diagram, i.e. at $-1 < \epsilon_L/U_{LR} = \epsilon_R/U_{LR} < 0$ on-site energy settings (brown line connecting the triple points in Fig. 4b). Therefore we studied the CPS efficiency $s = 2\Delta/(I_L + I_R)$ as a function of the inter-dot Coulomb repulsion at different locations in the stability map assigned by the markers in Fig. 4b, which are plotted in Fig. 4c. For simplicity, the charging energies were chosen as $U_L = U_R = U = 1$ meV and $\Delta = 0.2$ meV has been used.

As visible in Fig. 4c, s is significantly higher along the degeneracy line of the $|1, 0\rangle$ and $|0, 1\rangle$ sectors (pink triangle, blue square, yellow diamond) than anywhere else in the stability diagram, and maximal at $\epsilon_L/U_{LR} = \epsilon_R/U_{LR} = -0.5$, i.e. in the middle of the degeneracy line (blue square). This result is consistent with our experimental data where the non-local peaks were positioned to the center of the crossing resonance lines. By moving towards either of the triple points (pink triangle at $\epsilon_L/U_{LR} = \epsilon_R/U_{LR} = -0.8$), s decreases slightly. This small effect originates from the fact any of the CPS cycles that involves both the $|0, 0\rangle$ and the $|1, 1\rangle$

configurations as intermediate states (see the CPS process step (1) and (3) depicted in Fig. 4a), thereby being penalized by $\sim U_{LR}$. Obviously, by increasing U_{LR} the triple points separate further, hence suppressing s . We note that the calculations were performed at fixed $\epsilon_{L(R)}/U_{LR}$ ratios compensating the change of the length of the brown degeneracy line in Fig. 4b. Once one of the QDs is detuned from the resonance (at the gray circle and the green triangle with fixed $\epsilon_{L(R)}$), s drops significantly in accordance with the expectations as LPT starts to dominate the transport. Altogether, $U_{LR} \approx \Delta < 0.2$ meV relevant for our experimental values, the reduction of s does not exceed 10% compared to the non-interacting case. We note that similar results can be obtained at other on-site energy settings (e.g. in the vicinity of the $|1, 1\rangle, |2, 1\rangle, |1, 2\rangle$ and $|2, 1\rangle, |1, 2\rangle, |2, 2\rangle$ triple points) due to the symmetry of the charge stability diagram.

As a simple analysis, one can derive the maximal efficiency attainable in single-nanowire-based CPS by assuming the typical values of $\delta r \approx 300$ nm (see Fig. 1a) and $U_{LR} = 0$ (I.), and compare it to the calculation performed $U_{LR} = 0.15$ meV by assuming $\delta r = 30$ nm, reasonable for our setup (II., see Fig. 1a). According to Eq. (1), in the former case, $s_{\max}^I \approx 82\%$, while in the latter one $s_{\max}^{II} \approx 89\%$ in principle. By using these values, the geometry exhibiting a minimal δr , yet a finite U_{LR} turns out to be beneficial regarding the CPS efficiency. Naively one can argue it as $U_{LR} \propto 1/\delta r$ while s decays exponentially in δr as outlined in Eq. (1). This consideration with the relatively high CPS efficiency reported here in spite of the parasitic inter-dot Coulomb repulsion confirms the advantageous application of parallel InAs nanowires in future SC-semiconductor hybrids.

In summary, we have demonstrated significant Cooper pair splitting signals realized in parallel InAs nanowires connected by an epitaxial Al shell. The behavior of the coupled parallel SC-QD-N junctions was analyzed by spectroscopic measurements in both the superconducting and normal states. Owing to the geometrical properties, strong capacitive interaction was found between the QDs whose effect on the CPS was thoroughly studied. Due to the high-quality interface between the SC and semiconductor and the controlled QD formation, $s_{\max} = 29\text{--}36\%$ CPS efficiency was achieved larger than previously reported in parallel-wire-based experiments, which lacked these features³⁷. Our theoretical modeling also proved that regarding s_{\max} , the small spatial separation of QDs outgrow the drawbacks of the inter-dot Coulomb repulsion. The strong CAR makes the double-wire system with epitaxial shell a promising platform to develop quantum circuits designed to realize Majorana bound states¹⁴ or such exotic states as parafermions²⁷.

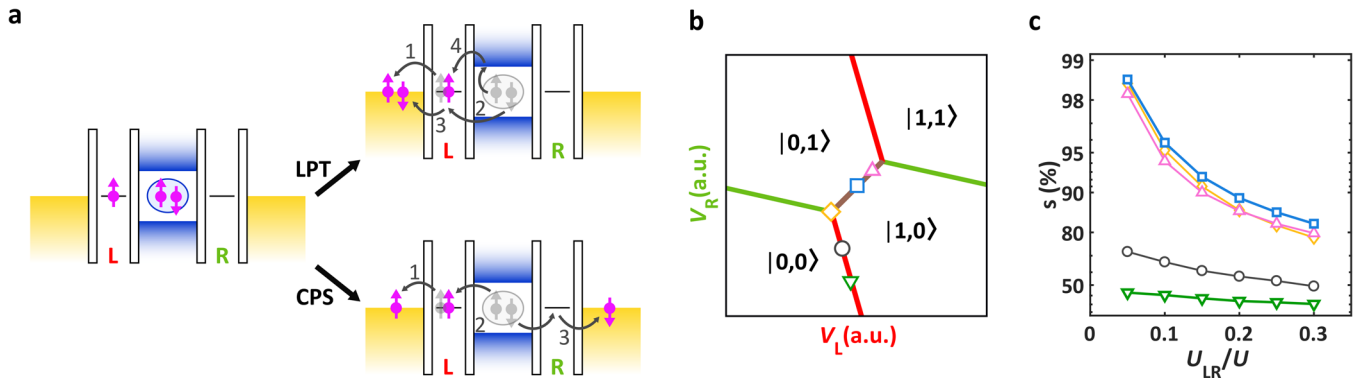


Fig. 4 | Transport modeling. **a** A possible sequence of LPT and CPS. The arrows with the numbers indicate the event order in the sequence. Electrons in gray symbolize the initial occupations, while the purple ones belong to the final states. **b** Sketched phase diagram of the honeycomb presenting the border of ground state occupations of both QDs simultaneously. By crossing the red (green) line, the electron number is changed on the left (right) QD. **c** U_{LR}/U dependence of s calculated in different points of the stability diagram, indicated by markers in panel (b). While a decreasing tendency of the CPS contribution to the total current can be observed throughout the phase diagram, the efficiency is maximal in the middle of the $|1, 0\rangle$ and $|0, 1\rangle$ degeneracy lines.

METHODS

Device fabrication

InAs nanowires were grown by MBE in the wurtzite phase along the (0001) direction catalyzed by Au. The pattern of the pre-defined Au droplets allowed to control the geometrical properties of the proposed parallel nanowires, including the diameter, distance, and the corresponding alignment of the cross-sections³⁹. The 20-nm-thick Al shell (covering 2 facets) was evaporated at low temperature in-situ providing epitaxial, oxide-free layers. The evaporation on such a pair of adjacent nanowires resulted in the merging by the Al. Nanowires with ~80 nm diameter, ~4 μm length, and ~200 nm seed separation were deposited on a p-doped Si wafer capped with 290 nm thick SiO₂ layer by using an optical transfer microscope with micromanipulators. The Al shell was partially removed by the means of wet chemical etching. A coated MMA/MAA EL-6 double-layer performed as a masking layer, in which designed windows were opened with EBL allowing the MF-321 selective developer to access the Al (45 s). The etching was followed by a careful localization of the wires with high-resolution SEM. The contact electrodes were installed in a separate EBL step with a thicker PMMA resist (300 nm), where the sample was exposed to RF Ar milling in the evaporator chamber to remove the native oxide of both the Al and InAs. The process was followed by the metallization of Ti/Au (10/80 nm) with electron beam evaporation without breaking the vacuum. In a second EBL step, the side gate electrodes were created by using thinner PMMA resist (100 nm) and depositing Ti/Au (10/25 nm).

Measurements

Low-temperature characterization was carried out in a Leiden Cryogenics dry dilution refrigerator with a base temperature of 40 mK. Transport measurements were performed with standard lock-in technique by applying 10 μV AC signal at 137 Hz on the shared SC electrode, whereas the differential conductance of the nanowires was recorded separately via home-built I/V converters. DC bias was adjusted by the offset of the I/V converters. Out-of-plane magnetic field was realized by a superconducting magnet. The QDs were formed by the outer finger gate electrodes with $V_{\text{TL}} = -3.5\text{ V}$, $V_{\text{BL}} = -1.6\text{ V}$, $V_{\text{TR}} = -6.5\text{ V}$, and $V_{\text{BR}} = 0\text{ V}$ values, where T(B) stands for top (bottom) and L(R) stands for left (right) labeling them by following the arrangement visible in Fig. 1d. Both large side gates on the top in Fig. 1d were set to $V_{\text{G}} = -2\text{ V}$ to slightly tune the electron density in the nanowire segments covered by the Al shell.

DATA AVAILABILITY

The data introduced and analyzed during the current study are available at <https://doi.org/10.5281/zenodo.6642304>.

CODE AVAILABILITY

The custom codes and mathematical algorithms used to evaluate the data are available at <https://doi.org/10.5281/zenodo.6642304>.

Received: 10 March 2022; Accepted: 10 August 2022;

Published online: 09 September 2022

REFERENCES

- Recher, P., Sukhorukov, E. V. & Loss, D. Andreev tunneling, Coulomb blockade, and resonant transport of nonlocal spin-entangled electrons. *Phys. Rev. B* **63**, 165314 (2001).
- Lesovik, G. B., Martin, T. & Blatter, G. Electronic entanglement in the vicinity of a superconductor. *Eur. Phys. J. B* **24**, 287–290 (2001).
- Recher, P. & Loss, D. Superconductor coupled to two Luttinger liquids as an entangler for electron spins. *Phys. Rev. B* **65**, 165327 (2002).
- Zazunov, A., Shumeiko, V., Bratus, E., Lantz, J. & Wendin, G. Andreev level qubit. *Phys. Rev. Lett.* **90**, 087003 (2003).
- Koch, J. et al. Charge-insensitive qubit design derived from the Cooper pair box. *Phys. Rev. A* **76**, 042319 (2007).
- Janvier, C. et al. Coherent manipulation of Andreev states in superconducting atomic contacts. *Science* **349**, 1199–1202 (2015).
- Hays, M. et al. Direct microwave measurement of Andreev-bound-state dynamics in a semiconductor-nanowire Josephson junction. *Phys. Rev. Lett.* **121**, 047001 (2018).
- Tosi, L. et al. Spin-orbit splitting of Andreev states revealed by microwave spectroscopy. *Phys. Rev. X* **9**, 011010 (2019).
- Kitaev, A. Y. Unpaired Majorana fermions in quantum wires. *Physics-Uspekhi* **44**, 131 (2001).
- Lutchyn, R. M., Sau, J. D. & Sarma, S. D. Majorana fermions and a topological phase transition in semiconductor-superconductor heterostructures. *Phys. Rev. Lett.* **105**, 077001 (2010).
- Oreg, Y., Refael, G. & Von Oppen, F. Helical liquids and Majorana bound states in quantum wires. *Phys. Rev. Lett.* **105**, 177002 (2010).
- Vaitiekėnas, S. et al. Flux-induced topological superconductivity in full-shell nanowires. *Science* **367**, eaav3392 (2020).
- Prada, E. et al. From Andreev to Majorana bound states in hybrid superconductor-semiconductor nanowires. *Nat. Rev. Phys.* **2**, 575–594 (2020).
- Leijnse, M. & Flensberg, K. Parity qubits and poor man's Majorana bound states in double quantum dots. *Phys. Rev. B* **86**, 134528 (2012).
- Mourik, V. et al. Signatures of Majorana fermions in hybrid superconductor-semiconductor nanowire devices. *Science* **336**, 1003–1007 (2012).
- Das, A. et al. Zero-bias peaks and splitting in an Al-InAs nanowire topological superconductor as a signature of Majorana fermions. *Nat. Phys.* **8**, 887–895 (2012).
- Deng, M. et al. Majorana bound state in a coupled quantum-dot hybrid-nanowire system. *Science* **354**, 1557–1562 (2016).
- Albrecht, S. M. et al. Exponential protection of zero modes in Majorana islands. *Nature* **531**, 206–209 (2016).
- Gül, Ö. et al. Ballistic Majorana nanowire devices. *Nat. Nanotechnol.* **13**, 192–197 (2018).
- Grivnin, A., Bor, E., Heiblum, M., Oreg, Y. & Shtrikman, H. Concomitant opening of a bulk-gap with an emerging possible Majorana zero mode. *Nat. Commun.* **10**, 1940 (2019).
- Hofstetter, L., Csonka, S., Nygård, J. & Schönenberger, C. Cooper pair splitter realized in a two-quantum-dot y-junction. *Nature* **461**, 960–963 (2009).
- Herrmann, L. et al. Carbon nanotubes as Cooper pair beam splitters. *Phys. Rev. Lett.* **104**, 026801 (2010).
- Hofstetter, L. et al. Finite-bias Cooper pair splitting. *Phys. Rev. Lett.* **107**, 136801 (2011).
- Schindele, J., Baumgartner, A. & Schönenberger, C. Near-unity Cooper pair splitting efficiency. *Phys. Rev. Lett.* **109**, 157002 (2012).
- Das, A. et al. High-efficiency Cooper pair splitting demonstrated by two-particle conductance resonance and positive noise cross-correlation. *Nat. Commun.* **3**, 1165 (2012).
- Deacon, R. S. et al. Cooper pair splitting in parallel quantum dot Josephson junctions. *Nat. Commun.* **6**, 7446 (2015).
- Klinovaja, J. & Loss, D. Time-reversal invariant parafermions in interacting Rashba nanowires. *Phys. Rev. B* **90**, 045118 (2014).
- Reeg, C., Klinovaja, J. & Loss, D. Destructive interference of direct and crossed Andreev pairing in a system of two nanowires coupled via an s-wave superconductor. *Phys. Rev. B* **96**, 081301 (2017).
- Thakurathi, M., Simon, P., Mandal, I., Klinovaja, J. & Loss, D. Majorana Kramers pairs in Rashba double nanowires with interactions and disorder. *Phys. Rev. B* **97**, 045415 (2018).
- Byers, J. M. & Flatté, M. E. Probing spatial correlations with nanoscale two-contact tunneling. *Phys. Rev. Lett.* **74**, 3305 (1995).
- Deutscher, G. & Feinberg, D. Coupling superconducting-ferromagnetic point contacts by Andreev reflections. *Appl. Phys. Lett.* **76**, 487–489 (2000).
- Leijnse, M. & Flensberg, K. Coupling spin qubits via superconductors. *Phys. Rev. Lett.* **111**, 060501 (2013).
- Tan, Z. et al. Cooper pair splitting by means of graphene quantum dots. *Phys. Rev. Lett.* **114**, 096602 (2015).
- Tan, Z. et al. Thermoelectric current in a graphene Cooper pair splitter. *Nat. Commun.* **12**, 138 (2021).
- Ranni, A., Brange, F., Mannila, E. T., Flindt, C. & Maisi, V. F. Real-time observation of Cooper pair splitting showing strong non-local correlations. *Nat. Commun.* **12**, 6358 (2021).
- Pandey, P., Danneau, R. & Beckmann, D. Ballistic graphene Cooper pair splitter. *Phys. Rev. Lett.* **126**, 147701 (2021).
- Baba, S. et al. Cooper pair splitting in two parallel InAs nanowires. *New J. Phys.* **20**, 063021 (2018).
- Ueda, K. et al. Dominant nonlocal superconducting proximity effect due to electron-electron interaction in a ballistic double nanowire. *Sci. Adv.* **5**, eaaw2194 (2019).
- Kanne, T. et al. Double nanowires for hybrid quantum devices. *Adv. Funct. Mater.* **32**, 2107926 (2022).
- Kürtössy, O. et al. Andreev molecule in parallel InAs nanowires. *Nano Lett.* **21**, 7929–7937 (2021).
- Vekris, A. et al. Josephson junctions in double nanowires bridged by in-situ deposited superconductors. *Phys. Rev. Res.* **3**, 033240 (2021).

42. Vekris, A. et al. Asymmetric Little–Parks oscillations in full shell double nanowires. *Sci. Rep.* **11**, 19034 (2021).
43. Vekris, A. et al. Electronic transport in double-nanowire superconducting islands with multiple terminals. *Nano Lett.* **22**, 5765–5772 (2022).
44. Estrada Saldaña, J. C. et al. Excitations in a superconducting Coulombic energy gap. *Nat. Commun.* **13**, 2243 (2022).
45. Fülöp, G. et al. Local electrical tuning of the nonlocal signals in a Cooper pair splitter. *Phys. Rev. B* **90**, 235412 (2014).
46. Fülöp, G. et al. Magnetic field tuning and quantum interference in a Cooper pair splitter. *Phys. Rev. Lett.* **115**, 227003 (2015).
47. Krogstrup, P. et al. Epitaxy of semiconductor-superconductor nanowires. *Nat. Mater.* **14**, 400–406 (2015).
48. Chang, W. et al. Hard gap in epitaxial semiconductor-superconductor nanowires. *Nat. Nanotechnol.* **10**, 232–236 (2015).
49. Walldorf, N., Padurariu, C., Jauho, A.-P. & Flindt, C. Electron waiting times of a Cooper pair splitter. *Phys. Rev. Lett.* **120**, 087701 (2018).
50. Walldorf, N., Brange, F., Padurariu, C. & Flindt, C. Noise and full counting statistics of a Cooper pair splitter. *Phys. Rev. B* **101**, 205422 (2020).
51. Brange, F., Prech, K. & Flindt, C. Dynamic Cooper pair splitter. *Phys. Rev. Lett.* **127**, 237701 (2021).
52. Buitelaar, M., Nussbaumer, T. & Schönenberger, C. Quantum dot in the Kondo regime coupled to superconductors. *Phys. Rev. Lett.* **89**, 256801 (2002).
53. Sand-Jespersen, T. et al. Kondo-enhanced Andreev tunneling in InAs nanowire quantum dots. *Phys. Rev. Lett.* **99**, 126603 (2007).
54. Eichler, A. et al. Even-odd effect in Andreev transport through a carbon nanotube quantum dot. *Phys. Rev. Lett.* **99**, 126602 (2007).
55. Grove-Rasmussen, K. et al. Superconductivity-enhanced bias spectroscopy in carbon nanotube quantum dots. *Phys. Rev. B* **79**, 134518 (2009).
56. Pillet, J. et al. Andreev bound states in supercurrent-carrying carbon nanotubes revealed. *Nat. Phys.* **6**, 965–969 (2010).
57. Eldridge, J., Pala, M. G., Governale, M. & König, J. Superconducting proximity effect in interacting double-dot systems. *Phys. Rev. B* **82**, 184507 (2010).
58. Lee, E. J. et al. Spin-resolved Andreev levels and parity crossings in hybrid superconductor-semiconductor nanostructures. *Nat. Nanotechnol.* **9**, 79–84 (2014).
59. Trocha, P. & Weymann, I. Spin-resolved Andreev transport through double-quantum-dot Cooper pair splitters. *Phys. Rev. B* **91**, 235424 (2015).
60. Hussein, R., Jaurigue, L., Governale, M. & Braggio, A. Double quantum dot Cooper pair splitter at finite couplings. *Phys. Rev. B* **94**, 235134 (2016).
61. Jellinggaard, A., Grove-Rasmussen, K., Madsen, M. H. & Nygård, J. Tuning Yu-Shiba-Rusinov states in a quantum dot. *Phys. Rev. B* **94**, 064520 (2016).
62. Scherübl, Z. et al. Large spatial extension of the zero-energy Yu-Shiba-Rusinov state in a magnetic field. *Nat. Commun.* **11**, 1834 (2020).
63. Sauret, O., Feinberg, D. & Martin, T. Quantum master equations for the superconductor-quantum dot entangler. *Phys. Rev. B* **70**, 245313 (2004).
64. Van der Wiel, W. G. et al. Electron transport through double quantum dots. *Rev. Mod. Phys.* **75**, 1–22 (2002).

ACKNOWLEDGEMENTS

The authors are thankful to EK MFA for providing their facilities for sample fabrication. We thank D. Olstein, M. Marnauza, A. Vekris, and K. Grove-Rasmussen for experimental assistance, A. Pályi, A. Virostek for discussion, M. G. Beckerne, F. Fülöp, and M. Hajdu for their technical support. This work has received funding Topograph FlagERA, the SuperTop QuantERA network, the FET Open AndQC, the FET Open SuperGate, the COST Nanocohybr network, and from the OTKA K138433 and OTKA

FK 132146 grants. G. F. acknowledges support from the Bolyai Fellowship. This research was supported by the Ministry of Innovation and Technology and the NKFIH within the Quantum Information National Laboratory of Hungary and by the Quantum Technology National Excellence Program (Project Nr.- 2017-1.2.1-NKP-2017-00001), UNKP-21-5 New National Excellence Program of the Ministry for Innovation and Technology from the source of the National Research, Development and Innovation Fund, and the Carlsberg Foundation, and the Danish National Research Foundation.

AUTHOR CONTRIBUTIONS

O.K. and I.L. fabricated the device, O.K., Z.S., and G.F. performed the measurements and did the data analysis. Z.S. built the theoretical model and developed the numerical simulations. T.K. and J.N. developed the nanowires. All authors discussed the results and worked on the manuscript. P.M. and S.C. proposed the device concept and guided the project.

FUNDING

Open access funding provided by Budapest University of Technology and Economics.

COMPETING INTERESTS

The authors declare no competing interests.

ADDITIONAL INFORMATION

Supplementary information The online version contains supplementary material available at <https://doi.org/10.1038/s41535-022-00497-9>.

Correspondence and requests for materials should be addressed to Olivér. Kürtösy, Péter Makk or Szabolcs Csonka.

Reprints and permission information is available at <http://www.nature.com/reprints>

Publisher's note Springer Nature remains neutral with regard to jurisdictional claims in published maps and institutional affiliations.



Open Access This article is licensed under a Creative Commons

Attribution 4.0 International License, which permits use, sharing, adaptation, distribution and reproduction in any medium or format, as long as you give appropriate credit to the original author(s) and the source, provide a link to the Creative Commons license, and indicate if changes were made. The images or other third party material in this article are included in the article's Creative Commons license, unless indicated otherwise in a credit line to the material. If material is not included in the article's Creative Commons license and your intended use is not permitted by statutory regulation or exceeds the permitted use, you will need to obtain permission directly from the copyright holder. To view a copy of this license, visit <http://creativecommons.org/licenses/by/4.0/>.

© The Author(s) 2022